Swansea University
Prifysgol Abertawe

Cronfa
Setting Research Free

Cronfa - Swansea University Open Access Repository

This is an author produced version of a paper published in :
Materials Science and Engineering: A

Cronfa URL for this paper:
http://cronfa.swan.ac.uk/Record/cronfa26485

Paper:
Coleman, M., Alshehri, H., Banik, R., Harrison, W. & Birosca, S. (2016). Deformation mechanisms of IN713C nickel based superalloy during Small Punch Testing. *Materials Science and Engineering: A, 650*, 422-431.

http://dx.doi.org/10.1016/j.msea.2015.10.056

This article is brought to you by Swansea University. Any person downloading material is agreeing to abide by the terms of the repository licence. Authors are personally responsible for adhering to publisher restrictions or conditions. When uploading content they are required to comply with their publisher agreement and the SHERPA RoMEO database to judge whether or not it is copyright safe to add this version of the paper to this repository.
http://www.swansea.ac.uk/iss/researchsupport/cronfa-support/

Materials Science & Engineering A 650 (2016) 422–431

Contents lists available at ScienceDirect

Materials Science & Engineering A

journal homepage: www.elsevier.com/locate/msea

Deformation mechanisms of IN713C nickel based superalloy during Small Punch Testing

M. Coleman *, H. Alshehri, R. Banik, W. Harrison, S. Birosca

Materials Research Centre, College of Engineering, Swansea University, Singleton Park, Swansea SA2 8PP, UK

ARTICLE INFO

Article history:
Received 28 July 2015
Received in revised form
14 October 2015
Accepted 15 October 2015
Available online 22 October 2015

Keywords:
EBSD
Small Punch
Nickel based superalloys
Local microstructure

ABSTRACT

The role of local microstructure is critical in materials performance and integrity in a cast alloy. The grain size and grain boundary distributions as well as local texture can create various microstructure/microtexture clusters that cause deformation localisation in the alloy. Inconel 713C nickel base superalloys are used as turbocharger turbine wheels for modern diesel engines, produced via investment casting. In such an alloy localised deformation is highly expected during service, as the strain distribution is not uniform in the component due to casting geometrical factors in addition to non-homogenous microstructure and microtexture in the cast alloy. In the current investigation Small Punch (SP) tensile tests were carried out on IN713C at room temperature and 650 °C in an air environment under stroke control at a rate of 0.02 mm/s. The fracture surface examination and microstructure characterisation as well as detailed texture analyses were performed using Scanning Electron Microscopy (SEM) and Electron Backscatter Diffraction (EBSD). Finite Element (FE) analysis of the SP test was also implemented to investigate the role of stress state on the local deformation. It was evident that microstructure parameters such as grain morphology and original texture existed in the disc were the most influential factors in governing the deformation texture in mixed columnar/equiaxed (transition) disc microstructure. Whereas, the temperature was the determining parameter in grain rotations and texture changes for wholly columnar disc microstructures.

© 2015 The Authors. Published by Elsevier B.V. This is an open access article under the CC BY license (http://creativecommons.org/licenses/by/4.0/).

1. Introduction

IN713C is a γ′ precipitation hardened cast nickel based superalloy that possesses excellent mechanical properties up to 800 °C. It also has excellent resistance to oxidation and thermal fatigue as well as good castability [1,2]. It is generally used in commercial diesel turbocharger components where in-service conditions can reach 760 °C with severe radial stresses caused by operating at 150,000 rpm [3]. The turbocharger wheel turbines are produced via the investment casting process using the lost wax method, resulting in a final component which has a good surface finish and a high degree of precision. However, the microstructure generated by this process is not homogeneous due to the different cooling rates throughout the mould [4–6]. The final microstructure consists of relatively small equiaxed grains at blade tips, columnar grains in the bulk of the blades and large equiaxed grains in the main bulk of the component. Some casting defects may also occur, such as gas porosity, shrinkage porosity, oxide defects and shell inclusions [7]. Acting as stress concentration points these defects add to the variation in life cycles observed in stress versus life (S–N) data of the cast components [8–10]. When the stress at these concentration points reaches a critical level, fatigue cracks may initiate and propagate under the stress cycles that these components are subjected to during service.

In general, there is uncertainty in literature about the exact influence of each microstructural parameter, including porosity, inclusions, grain orientation and slip activity on crack initiation and propagation in IN713C cast alloy. Recent advancements in materials processing techniques and heat treatments have reduced cast defects and have greatly minimised their influence on the fatigue life of the components. Consequently, the roles of microstructure, grain boundary characteristics and local texture have subsequently become predominant factors in crack formation, growth and crack path during loading. Applications of recent modelling theories have extended to polycrystalline nickel superalloy, where material microstructure was considered as one of the major factors influencing the fatigue property of the material [11–16]. In a complex system such as cast IN713C alloy, these microstructural parameters should be identified and quantified to obtain a complete description of the alloy's deformation mechanism.

Investigating and characterising the inhomogeneous microstructures in such complex components is extremely challenging,

* Corresponding author.
E-mail address: m.p.coleman@swansea.ac.uk (M. Coleman).

http://dx.doi.org/10.1016/j.msea.2015.10.056
0921-5093/© 2015 The Authors. Published by Elsevier B.V. This is an open access article under the CC BY license (http://creativecommons.org/licenses/by/4.0/).

as sampling and preparation of conventional test samples is limited by component geometry. Small Punch (SP) testing allows for sampling of relatively small discs (9.5 mm diameter) from various areas of the component, allowing for mechanical testing of discrete areas of the component. Predominantly developed as a method for testing small volumes of material from nuclear reactors [17], SP testing has become more widely utilised during recent times. Numerous assessments are carried out in order to evaluate time-independent material properties associated with uniaxial tensile behaviour and toughness [18], accordingly this method is now widely utilised [19]. In comparison to conventional uniaxial tensile/compression tests, SP testing is a dynamic test with multiple deformation mechanisms operating simultaneously. However, despite the dynamic nature of SP testing, yield strength, ultimate tensile strength and tensile elongation can be predicted using the European Code of Practice 2007 [20], which details the most suitable test approaches as well as formula for the calculation of mechanical properties from the SP load/displacement data [21].

This investigation utilises small punch disc testing as a technique for evaluating the mechanical properties of different areas in turbo charger turbine wheel components. The microstructures of IN713C alloy at room temperature and high temperature (650 °C) are tested by means of SP and characterised using Electron Backscatter Diffraction (EBSD). The deformation mechanisms and possible causes of crack initiation and propagation are investigated.

2. Materials and methods

As cast IN713C components were supplied by Cummins Turbo Technologies Ltd/Huddersfield/UK, with the chemical composition shown in Table 1. Macro grain etching was carried out by submerging the component in an etchant consisting of 100 parts HCl (40%) to 14 parts H_2O_2 (30%) for 10 min in order to identify different microstructural zones for sampling, see Fig. 1(a and b). Samples were machined from three areas of two blades using wire Electric Discharge Machining (EDM) to produce 9.5 mm diameter discs, see Fig. 1(c and d). These small discs retained a slightly curved profile so were mounted in conductive phenolic compound and polished to provide a flat starting surface. The sample was then removed and successively polished with abrasive paper, using a hand lapping tool designed to hold the small disc, to a thickness of 0.5 mm $\pm$ 5 μm. The hand lapping tool relied on the sample sitting flat in the holder, therefore the previous stage of creating a flat starting surface was essential. Four small discs were successfully produced, one from the bottom (transition, *i.e.*, equiaxed/columnar region) and one from the middle (columnar region), see Fig. 1(e and f). The curved profile at the blade tip meant that small discs from these regions were unobtainable.

The SP tensile tests were performed on miniature discs, according to the European Code of Practice (CoP) for Small Punch Testing [20]. A bespoke small punch jig with a 4 mm punch head diameter was used in conjunction with a Zwick servo-actuated electric-screw testing machine to perform the mechanical testing. For high temperature testing a Severn Furnaces split-tube furnace connected to a Eurotherm controller unit was used to heat the sample to 650 °C with a soak time of 1 h. The testing temperature of 650 °C was selected to emulate approximate operating temperature in turbochargers where IN713C area mainly used. Disc temperature was monitored using a thermocouple in direct contact with the underside of the disc. Tests were performed in stroke control at a rate of 0.02 mm/s with load/displacement curves monitored during the test, and continued until disk fracture was evident.

Table 1
Chemical composition of IN713C alloy (wt%).

Element	Ni	Cr	Al	Mo	Nb	Fe	Ti
wt%	68.34	14.32	6.65	4.43	3.5	1.24	0.96

Following the sample failure, the SP discs were imaged using a Keyence light microscope linked to a Z-controlled stage. The failed small punch discs were sectioned in half and mounted on end so that the fracture surface could be polished for SEM analysis. Sectioned specimens were metallographically prepared using standard method, culminating with 0.05 μm Colloidal Silica for 20 min. Data were collected using a Nordlys EBSD detector and HKL Technology Channel 5 EBSD system interfaced to a Phillips XL30 Tungsten electron microscope operated at 20 kV.

Furthermore, in order to understand the stress state influences on the deformation texture, Finite Element Analysis (FEA) of the small punch test were performed. Analyses were run using the commercially available FEA solver Abaqus/Standard and due to symmetry of the disc, an axisymmetric model was used with CAX4 elements. Uniaxial material properties for IN713C were taken from literature [21] with an elastic modulus, $E=193$ GPa and Poisson's ratio, $\nu=0.3$. Isotropic plasticity was used with the Johnson-Cook hardening model:

$$\sigma^0 = A + B(\bar{\varepsilon}^{pl})^n \quad (1)$$

where σ^0 is the yield stress and $\bar{\varepsilon}^{pl}$ is the equivalent plastic strain, with parameters $A=380$ MPa, $B=603.6$ MPa and $n=0.0934$. The punch, clamp and disc holder were modelled as rigid bodies with a friction coefficient of 0.3 between all contact pairs. It should be noted that no damage or failure criterions were used in this FEA simulation. The punch, clamp and disc holder were modelled as rigid bodies with a friction coefficient of 0.3 between all contact pairs. It should be noted that no damage or failure criterions were used in this FEA simulation.

3. Results and discussion

3.1. Original microstructure observation

Fig. 2(a) shows an EBSD derived Inverse Pole Figure (IPF)// Loading Direction (LD) map of the original microstructure at the tip of a blade. It is evident from Fig. 2 that the corner of the blade tip consists of small equiaxed grains having relatively random texture. Fig. 2(b) and (c) shows EBSD maps for the entire small punch discs in Fig. 1(e) and (f), respectively. The microstructure shown in Fig. 2(b) consist of small equiaxed grains with a grain size of <500 μm transitioning to a larger, more columnar type microstructure, *i.e.*, transition microstructure. Whilst, the observed microstructure in Fig. 2(c) consists of a wholly columnar microstructure with grains several millimetres in length and width. It is evident from the figures that in both microstructures the grain boundaries are severely serrated in order to improve fatigue and creep resistance [22–24]. The Orientation Distribution Function (ODF) plots for Fig. 2(b) show that the original texture of the fine equiaxed grains consist of Goss $(011)<100>$, Rotated Cube $(001)<110>$, 5° away from Brass $(011)<112>$ and $(013)<100>$ texture components. Whereas, the original texture of the large columnar SP disc mainly consists of Cube $(001)<100>$ and rotated Cube $(001)<110>$ texture components, see Fig. 2(c).

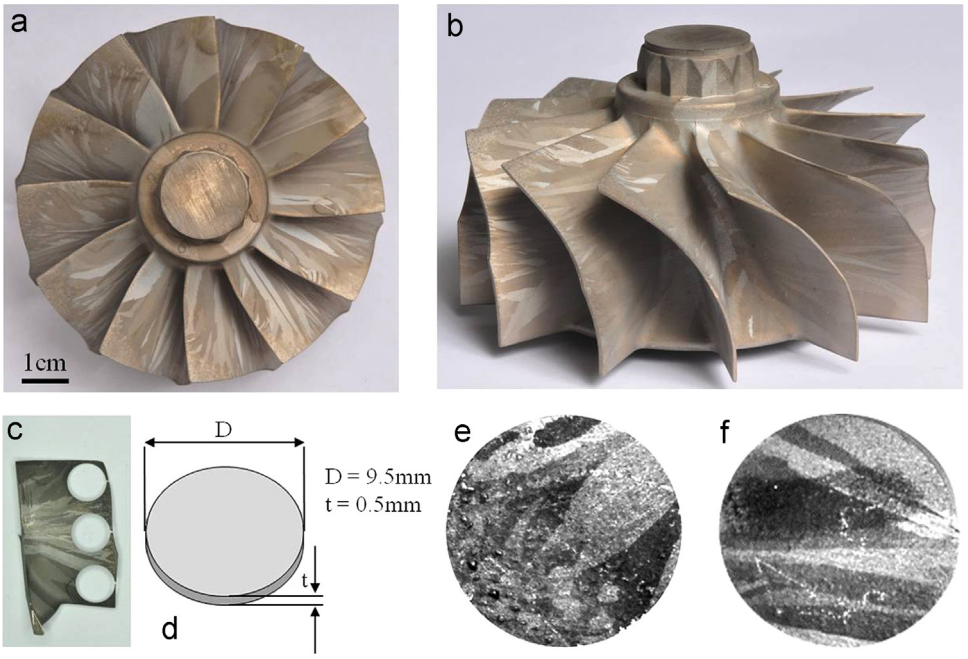

Fig. 1. (a) and (b) As-Received IN713C turbine component after macro etching, (c) removal of selected blade and SP sampling using Wire EDM, (d) schematic of SP disc, (e) optical micrograph of T-RT and (e) C-RT.

3.2. Small Punch Test

Two SP tests were performed at Room Temperature (RT), one disc from the bottom corner of the blade which has Transition (T) microstructure; T-RT, and the other from the middle of the blade which has Columnar (C) microstructure, C-RT. Further two more specimens were tested at 650C, *i.e.*, High Temperature (HT) for both microstructures; T-HT and C-HT. The load/displacement curves are shown in Fig. 3 and a summary of the yield load, upper load limit and maximum displacement are reported in Table 2. The tensile yield strength (σ_{ys}), Ultimate Yield Strength (σ_{UTS}) and elongation (A (%)) were calculated using the following equations [25]

$$\sigma_{ys} = \alpha_1 \frac{F_e}{t^2} + \alpha_2 \tag{2}$$

$$\sigma_{UTS} = \beta_1'' \frac{F_m}{(t d_m)} + \beta_2'' \tag{3}$$

$$A(\%) = \gamma' \frac{d_m}{t} \tag{4}$$

where α_1, α_2, β_1'',β_2'' are constants proposed by Ruan et al. [26] and Fleury and Ha [27] and depend on material type and the coefficient of friction between the SP indenter and the sample (α_1=0.4, α_2=0.38, β_1''=77 and β_2''=218. F_e=yield load, F_m=upper load limit, d_m=max. displacement before the onset of failure, t=SP sample thickness which is 0.5 mm in this case. γ'=14 and is a normalised empirical constant linked to the sample thickness (t) proposed by Rodriguez, et al., [28].

Fig. 3(a) shows the configuration schematic for the SP tests

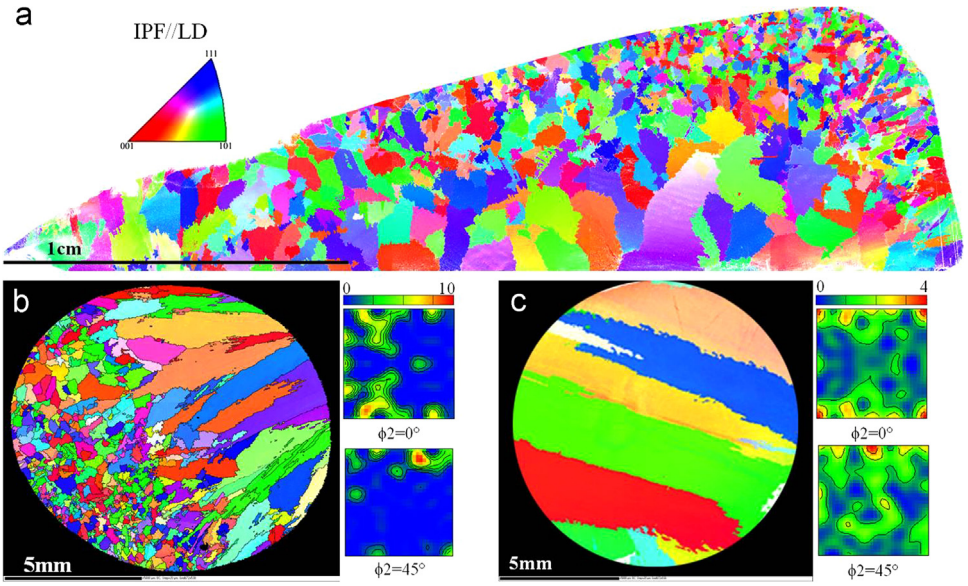

Fig. 2. EBSD IPF orientation map of (a) blade tip and IPF and ODF of (b) small punch transition disc and (c) columnar disc.

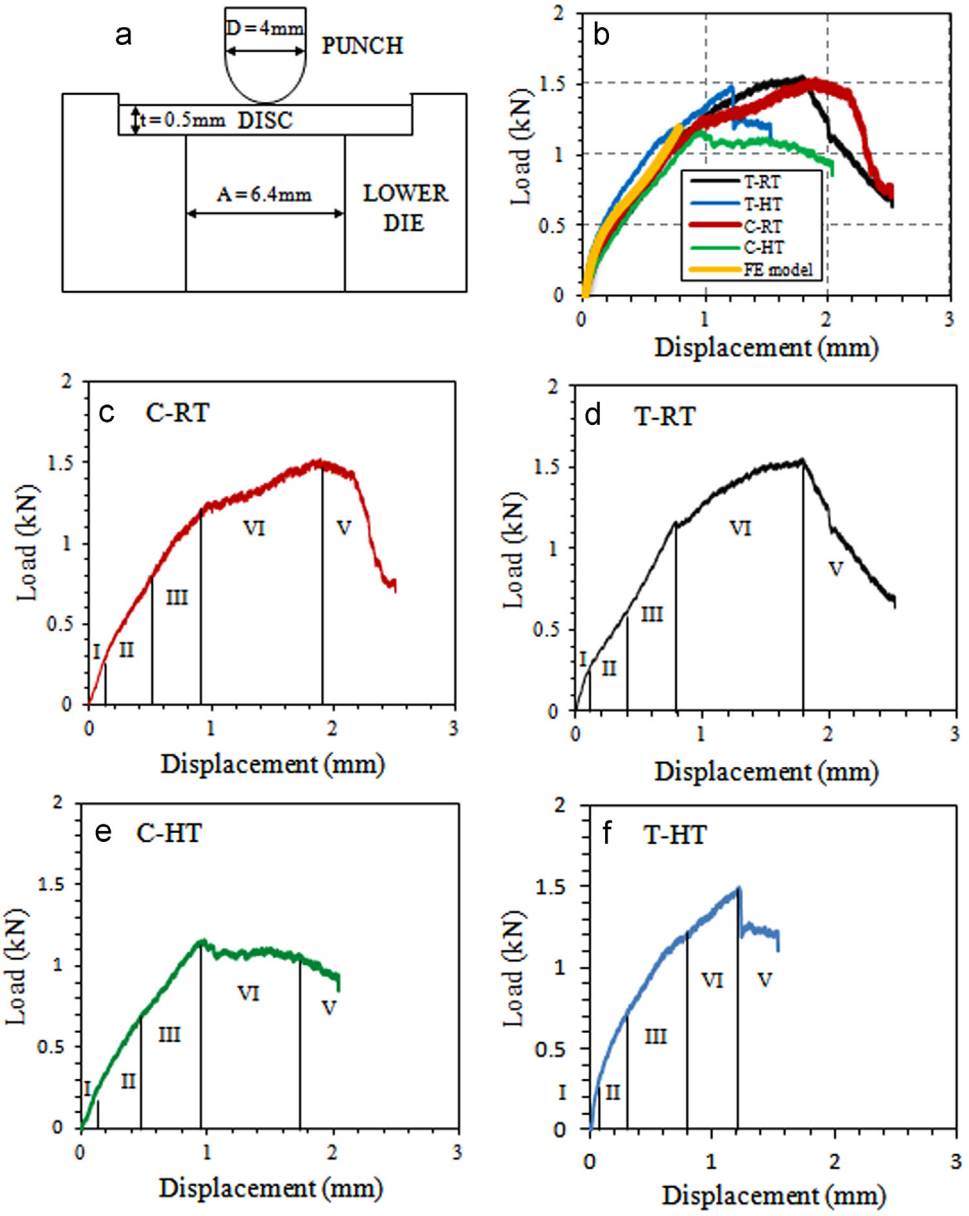

Fig. 3. Load–displacement curves of SP specimens (a) SP set up schematic (b) combined SP curves, (c) C-RT, (d) T-RT (e) C-HT and (f) T-HT.

Table 2
Summary of load/displacement data for SP.

Sample	Yield load kN (F_e)	Upper load limit kN (F_m)	Max dis mm (d_m)	σ_{ys} (MPa)	UTS (MPa)	*A%*
C-RT	0.22	1.52	1.9	880	1600	53.2
T-RT	0.21	1.55	1.8	840	1722	50.4
C-HT	0.15	1.16	1.8	600	1289	50.4
T-HT	0.18	1.49	1.2	720	2463	33.88

conducted at RT as well as HT and Fig. 3(b–f) show load/displacement curves for all the tested specimens. As described in literature [29–31] the load/displacement curve can be divided into four regions of deformation behaviour: namely; Region I (elastic bending), Region II (plastic bending), Region III (plastic membrane stretching) and Region VI (plastic instability). As the punch makes contact with the disc elastic bending occurs as appeared in Region I, see Fig. 3(b–e), followed by plastic deformation after yielding; Region II. The transition between Region I and II is defined as the vertical projection from the crossing points of two tangents extrapolated from the elastic regime and the plastic regime [20,28]. The load is then transferred to close non-yielding parts of the disc and causes the yield front to propagate through the entire thickness of the SP disc. As plastic deformation continues, the contact area between the disc and the punch head increases and the deformation mechanism changes from bending to stretching, Region III. This indicates the onset of membrane stretching where the material's strain hardening ability overcomes the reduction in thickness caused by stretching and enables it to sustain load at increasing rate [32]. On the load displacement curves the beginning of Region III is defined as the point at which the gradient of the curve increases. This phenomenon continues until instability occurs within the bulk material resulting in further decreasing resistance to deformation, Region IV, see Fig. 3. The onset of Region IV is defined from the decrease in the slope of the load displacement curve.

As shown in Fig. 3(c and d) and Table 2, the plasticity onset and membrane stretching regions, *i.e.*, Regions I, II and III are very similar in C-RT and T-RT specimens. These similarities were also

observed by others [31–33]. However, it is clear from the same figure that the load required to hold the SP disc in Region IV in T-RT was greater than C-RT specimen. It was evident that the equiaxed-columnar transition microstructure in T-RT disc could resist further plastic deformation and crack propagation compared to the columnar microstructure in C-RT disc. This is related to the higher number of grain boundaries in the equiaxed area being able to resist crack propagation. Once the stress reached a critical value the entire disc could not sustain under continuous load increment and failure occurred in the T-RT disc at the equiaxed/columnar interface resulting in rapid crack propagation and sudden failure without necking, see Region V in Fig. 3(d). Conversely, the columnar microstructures lowered the applied load in Region V and typical necking occurred before complete failure. The same observation is noticed for the specimens tested at HT, where the transition microstructure (T-HT) performed better than columnar microstructure (C-HT) until region IV. This is more related to better strength as a result of the equiaxed microstructure on one side of the SP disc, which provided crack retardation in that area.

It is also clear from Table 2, that due to materials softening and increased ductility the specimens tested at high temperatures (C-HT, T-HT yield load: 0.15, 0.18 KN, respectively) yielded much earlier than the specimens tested at room temperature (C-RT, T-RT yield load: 0.22, 0.21, respectively). Furthermore, the maximum displacement for the SP disc tested at RT (C-RT = 1.9 mm, T-RT = 1.8 mm) were greater than for the SP disc tested at HT (C-HT = 1.8 mm, T-HT = 1.2 mm). This is also reflected in the yield strength decreasing from 880 and 840 MPa in the samples tested at RT, *i.e.*, C-RT and T-RT, to 600 and 720 MPa in the samples tested at HT, *i.e.*, C-HT and T-HT, respectively. It appears that the IN713C tested at HT, reduced its strength at region IV dramatically with the C-HT disc continuing to resist failure until a final displacement of 1.8 mm, whereas the T-HT disc failed unexpectedly due to crack bifurcation as will be shown in Section 3.4. The initial superior performance of T-HT disc may be due to strain hardening effect of equiaxed grains in the transition microstructure. This is evident in the increase of UTS between the room temperature samples C-RT and C-HT of 1600 MPa and 1289 MPa respectively to 1722 MPa and 2484 MPa for the T-RT and T-HT high temperature samples. However, the plastic deformation and materials stretching reached the entire areas of the transition discs including the columnar side, therefore the disc could not continue under increased load in the phase instability region, Region IV, and failed unexpectedly due to an easy crack path provided by the boundary between the equiaxed and columnar areas as shown in Fig. 3(f). It should be noted that the equations used to determine the UTS and percentage elongation (A%), *i.e.*, Eq. (3) and Eq. (4) respectively, failed to accurately estimate these values. The industrial specification for this alloy expects a UTS in the region of 800–900 MPa and a percentage elongation of 10–15% [34,35]. The difficulty in estimating the maximum displacement before the onset of failure (d_m = max) as well as determining the effects of the membrane stretching and plastic instability regimes has over-estimated both the UTS and A% in this case (See Table 2). It is therefore useful to simulate the deformation mechanism using finite element modelling. However, this type of modelling does have a limitation as it assumes an isotropic microstructure throughout the SP disc. It is therefore essential to consider both the modelling results and the EBSD microstructural data concurrently.

3.3. Finite element analysis

As shown in Section 3.2, the equations 2–4 are correlating the load and displacement values from the SP tests to uniaxial tensile strength, UTS and elongation data. However the stress state in the SP test is complex and evolves throughout the test requiring a more complex analysis. Finite element analyses have been used to evaluate the stress as punch displacement increases. Fig. 4(a–d) shows the evolution of the von-Mises effective stress, $\bar{\sigma}$, during SP testing of IN713C at 650 °C with punch displacements of 0.25, 0.5, 0.75 and 1.0 mm, respectively. At punch displacements >1 mm load/displacement curves show the beginning of Region IV in most cases, which signifies the onset of instability in the microstructure leading to cracking. The model predicts continuum stress/strain behaviour whereas cracking is microstructurally sensitive and vary with repeated testes, therefore displacements greater than 1 mm were not included here. Since σ_{ys} and σ_{UTS} for IN713C at 20 °C and 650 °C are similar (within 2.5%), the difference in results of the stress analyses at both temperatures are negligible, therefore only results at 650 °C are shown here. Due to the symmetry in the disc, the global cylindrical coordinate system was used and $\bar{\sigma}$ is given as;

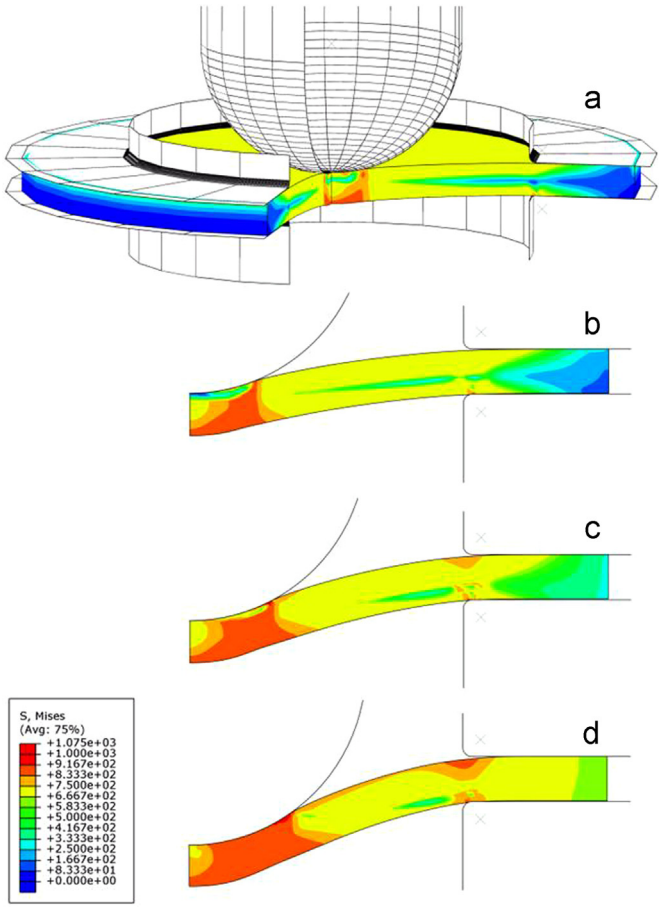

Fig. 4. Evolution of von-Mises stress during SP test with punch displacements of (a) 0.25 mm, (b) 0.5 mm, (c) 0.75 mm and (d) 1.0 mm.

$$\bar{\sigma} = \sqrt{\frac{1}{2}[(\sigma_{zz} - \sigma_{rr})^2 + (\sigma_{rr} - \sigma_{\theta\theta})^2 + (\sigma_{\theta\theta} - \sigma_{zz})^2] + 3(\sigma_{rz}^2)} \quad (5)$$

where σ_{zz}, σ_{rr} and $\sigma_{\theta\theta}$ are the axial, radial and hoop stresses, respectively. σ_{rz} is the active shear stress. The model is axisymmetric about the z-axis therefore $\sigma_{z\theta}$ and $\sigma_{\theta r}$ can be ignored. Upon initial loading there is high compressive stress immediately below the punch resulting in localised yielding, see Fig. 4(a). As punch displacement increases, the area of punch contact widens and the region of maximum $\bar{\sigma}$ propagates away from the centre of the disc, Fig. 4(b–d). This is consistent with deformation and stress predicted by Chang et al. [32] and Blagoeva and Hurst [36].

Further investigation of the stress state was carried out by

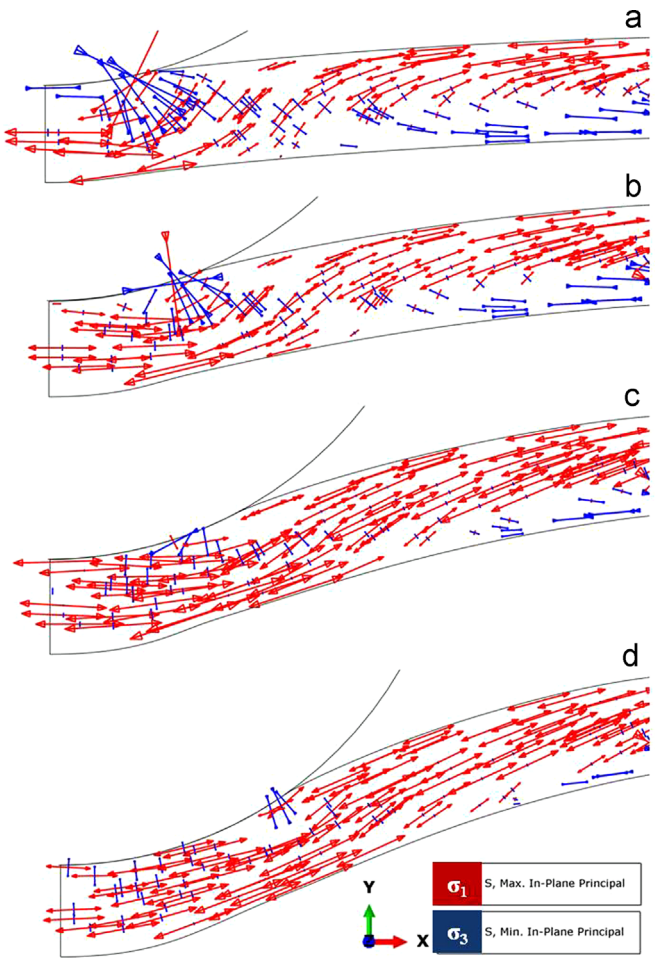

Fig. 5. Maximum (σ_1) and minimum (σ_2) principle stresses in IN713C disc at 650 °C during SP test with punch displacements of (a) 0.25 mm, (b) 0.5 mm, (c) 0.75 mm and (d) 1.0 mm.

plotting the principle stresses throughout the SP test, see Fig. 5. It is clear from the figure that there is a high compressive stress while punch displacement is $\leq$0.5 mm and it has a maximum value at the punch/disc interface, see Fig. 5(a and b). As the punch/disc contact area increases, the peak compressive stress (minimum principle stress, σ_3) decreases and moves away from the disc centre, see Fig. 5(c and d). The maximum principle stress, σ_1, is initially high on the underside of the disc at the disc centre and on the upper side in the clamped region, see Fig. 5(a). As deformation continues, σ_1 increases in the intermediate region and the stress in the disc becomes more tensile, see Fig. 5(c and d). This correlates well with 0.5–1 mm displacement Region III (plastic membrane stretching) observed in load/displacement plots (Fig. 3). Overall, the magnitude of stress in the disc is sufficient for yielding to occur. Furthermore, the predicted accumulation of plastic strain in the disc during testing is shown in Fig. 6. This figure shows that as punch displacement increases, the region of maximum shear plastic strain, ϵ_{rz}^{pl}, occurs in the disc adjacent to the location of punch contact. Noteworthy is the lack of shear plastic strain in the centre of the disc.

3.4. Specimen failure examination

Although the difference in results of the finite element stress analyses at RT and HT temperatures was negligible it is clear from Fig. 7, that the fracture surface and crack path were different between RT and HT discs. It is essential then that microstructural characteristics be considered in conjunction with the finite element model, since the model cannot simulate crack initiation and propagation, it seems that the failure mechanism is strongly correlated to the microstructural features. For the RT discs, Fig. 7(b) it appears that there is a primary crack with perpendicular secondary crack, giving a T-Shaped final cracked specimen. It appears that in the columnar microstructure of C-RT disc a microstructural feature such as a high angle grain boundary has resisted secondary crack propagation leading to further crack bifurcation, giving H-Shape cracked specimen, as indicated in Fig. 7(a). This crack

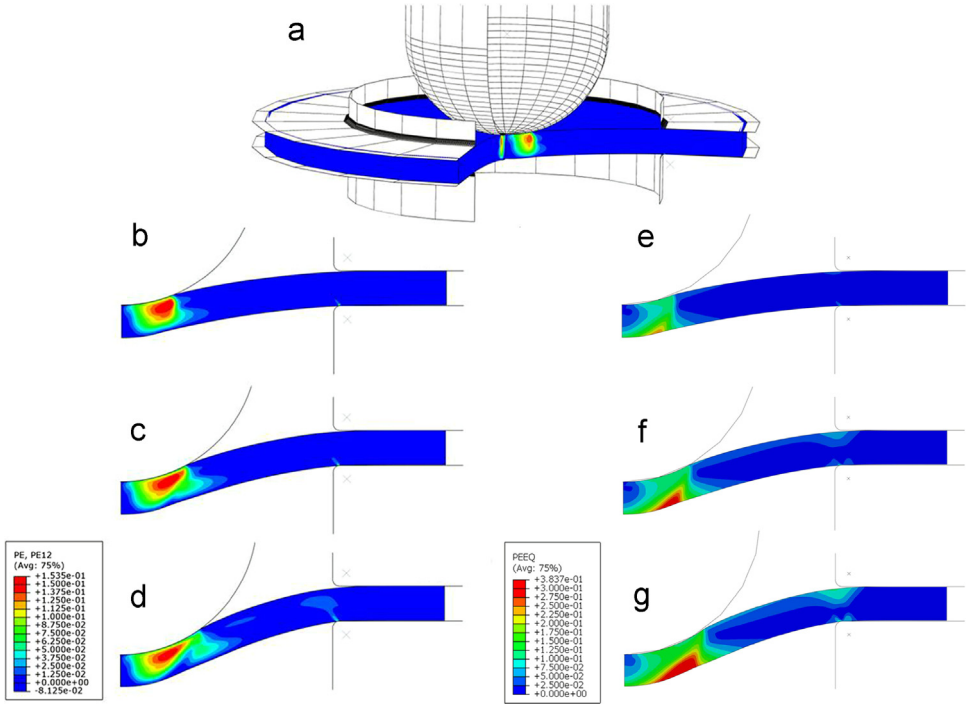

Fig. 6. Evolution of shear plastic strain, ε_12pl, during SP test with punch displacements of (a) 0.25 mm, (b) 0.5 mm, (c) 0.75 mm and (d) 1.0 mm. The equivalent plastic strain for punch displacements (e) 0.5 mm, (f) 0.75 mm and (g) 1.0 mm respectively.

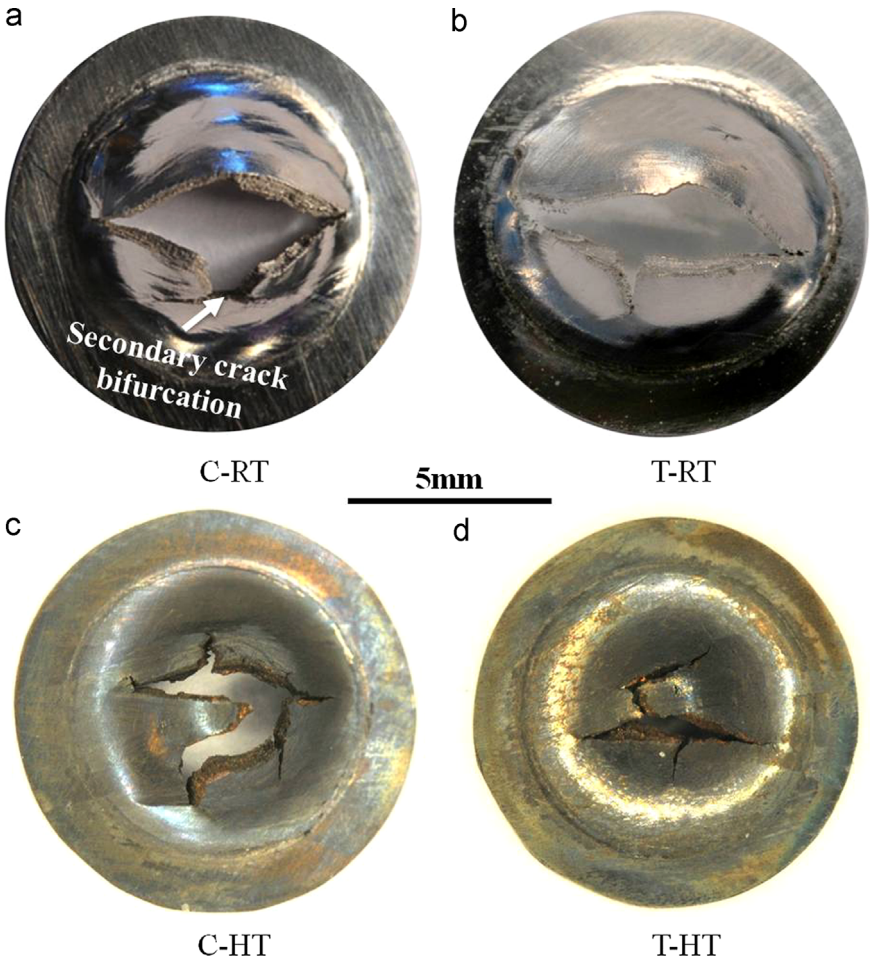

Fig. 7. Optical images of SP fractured discs of (a) C-RT, (b) T-RT and (c) C-HT and (d) T-HT.

retardation and bifurcation extended Region V as showed earlier in Fig. 3(c). Whereas in T-RT disc the primary and secondary cracks propagated without crack retardation, causing disc failure straight after reaching region V, see Fig. 3(d).

Due to materials softening effects at high temperature two or more major cracks appear with several secondary cracks, giving near V-Shape or X-Shape cracked specimens, see Fig. 7(c and d). This resulted in T-HT disc failing immediately after Region V, see Fig. 3(f). It is evident from Fig. 7(d) that two of the major cracks propagated easily in the columnar side of the transition (T-HT) microstructure, whereas the crack retarded in the equiaxed side of the disc. Whereas in the fully columnar disc of C-HT, Fig. 7(c), the major crack propagated dramatically in all directions resulting in a load reduction and an extension of Region IV, see Fig. 3(e). As shown in Fig. 7 an oxide scale was developed on the discs tested at HT giving the failed disc a brown colour. This may also assisted in fast crack advancement and shorter life in C-HT and T-HT specimens to some extent.

3.5. EBSD microstructure characterisation and texture analysis

Following the SP tests, the discs were cut in cross-section to reveal the fracture surfaces of the failed samples. One half of each fracture surface plane was then mounted and polished for EBSD analysis. EBSD derived IPF maps are reported in Fig. 8 where IPF colouration is aligned according to the nominal punch/load direction (LD), *i.e.* Y direction. From the IPF maps, it can be seen that there is an orientation change of the large grains from the SP disc edges to the central punch head contact region under loading. This is more related to slip system activation aspects in FCC materials and has caused deformation band formation that can be seen in cross-section, see Figs. 8(a) and (c). Fig. 8(b) shows the C-RT sample disc in cross section where the disc sides have a strong $<110>$//LD texture, which changes to a $<001>$//LD texture at the central punch head contact region. The T-RT sample, Fig. 8(d), has a $<110>$ and $<112>$//LD texture at the disc sides and a strong $(001)<100>$ texture component in the central region of the deformed disc. Moreover, both C-HT and T-HT discs, have $<111>$, $<110>$, $<100>$ and $<112>$//LD texture components at the sides and $<110>$ and $<112>$//LD texture in the central region, see Fig. 8(e and f). In most cases it can be seen that there is a tendency of an orientation change from the original orientation at the side/grip region to a $<110>$ orientation in the region between the grip and the tip of the punch head for the specimens tested at RT. This is unsurprising since it is generally believed that slip occurs on the most densely packed planes and in the most densely packed directions, which in the case of Ni is the {111} plane and in the $<110>$ direction [37]. The region between the punch tip and the die, *i.e.* the area where membrane stretching is most likely to occur, is similar to the deformation texture observed during extrusion of another FCC material such as gold [38]. It appears that the $<110>$//LD and $<112>$//LD fibre textures was formed at the contact points between the material and the extrusion nozzle similar to the one formed between the punch tip and the die during SP test. These regions of greatest orientation change also correspond to the areas of highest deformation rates and stress values as modelled and reported in Section 3.3, see also Figs. 4 and 6. This simulation result is in agreement with other

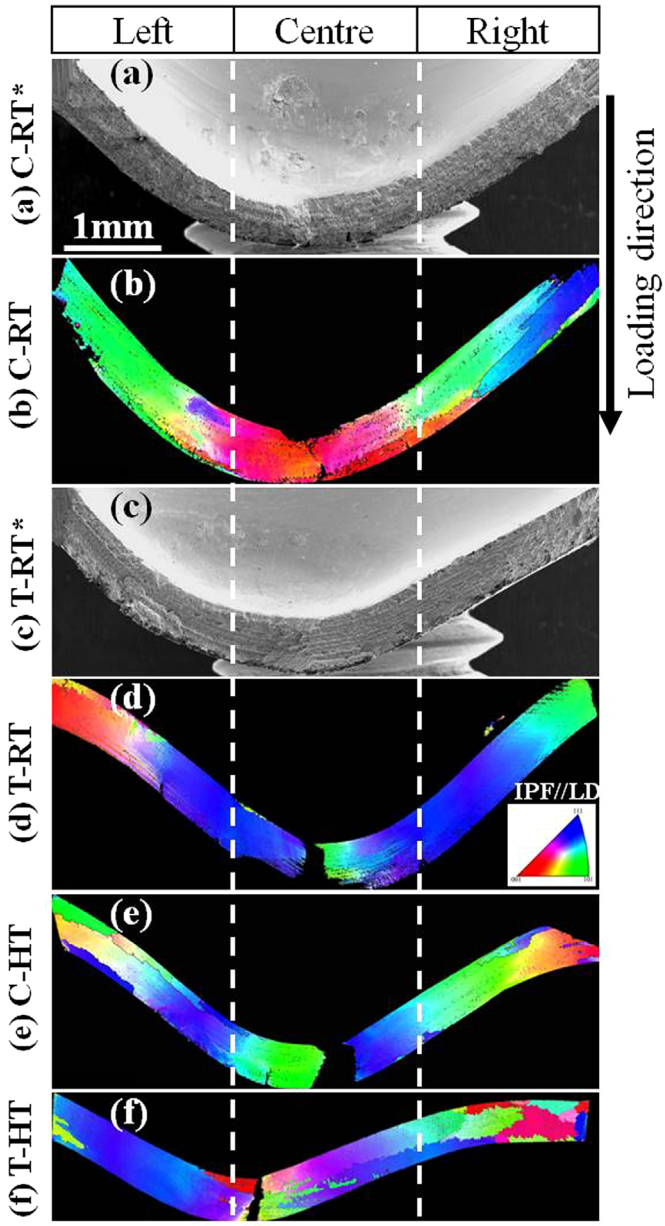

Fig. 8. SEM image of (a) C-RT* and (c) T-RT* fracture surfaces and EBSD IPF orientation maps of SP cross-sections (b) C-RT, (d) T-RT, (e) C-HT and (f) T-HT.

modelling results by Chang et al. [32] and Blagoeva and Hurst [36]. It is also evident that the $<110>$//LD texture formation in this region which caused membrane stretching were completely under tension as shown in Fig. 5. As reported in Section 3.2, the deformation mechanism changes from bending to stretching, *i.e.*, Region III, where stress continues to increase during the punch. The onset of membrane stretching during punch test is important for the material's strain hardening in order to overcome the reduction in thickness and enables it to sustain load at increasing rates.

As reported in Section 3.1 (Fig. 2) the original texture of the fine equiaxed area in the SP disc was different from the original texture of the lager columnar SP disc. However, the EBSD derived Orientation Distribution Function (ODF) plots showed that the texture components in the C-RT and T-RT discs following the test at room temperature remained the same within 5–10° deviations. As shown in Fig. 9(a), the $(001)<110>$ Rotated Cube ($\pm 5°$) on the left and right sides on the punched disc remained unchanged from the original texture component, see also the ODFs in Fig. 2(c). Furthermore, the Cube $(001)<100>$ texture components in the original sample was persisted in the centre of the C-RT sample following the SP test with a deviation of $\pm 4°$, see Fig. 9(a). Similar observation found in T-RT disc, where Rotated Cube and $(011)<112>$ Brass texture components that originally existed in transition microstructure disc, see Fig. 2(b), are persisted with a deviation of $\pm 9°$ after SP test on the left and right hand sides of the punched disc, where the $(011)<100>$ Goss remained with a deviation of $\pm 7°$ in the centre, see Fig. 9(b). This indicates that although the microstructure of the C-RT and T-RT were changed and the deformation bands were generated during the tests, see Fig. 8(a), the existing texture components have provided pure shear on $<110>$ direction without rotation of the entire grains during the deformation process. From the stress and strain evolution maps in Figs. 4–6, it is clear that the centre of the disc has minimum von-Mises stress and shear plastic stain at 0.5, 0.75 and 1 mm punch displacements. Furthermore, the centre is under tensile stress at those punch displacements. This stress states provided further enhancement of $<001>$//LD in both C-RT and T-RT discs which reflected in $(001)<100>$ Cube and Goss $(011)<100>$ texture components in the centres of C-RT and T-RT disc, respectively. The sides of the discs are under tension and compressive stress, see Fig. 5, with maximum von-Mises stress and shear plastic stain at 0.5, 0.75 and 1 mm punch displacements. This state provided pure shear $<110>$//LD and enhanced the existing $(001)<110>$ R-Cube texture component on the side of both C-RT and T-RT discs. Therefore, the original texture components were strengthened during RT test with no need for orientation changes. It should be emphasised here, the $(001)<112>$ Brass texture component also persisted in the T-RT disc sides as there is tension only or compression only regions in the underside of the disc side, see again Fig. 5(b). However, this was not the case for the SP discs tested at high temperature, *i.e.*, 650 °C. The original Cube and Rotated Cube texture components in the disc with columnar microstructure were transformed to Goss and Brass texture (with $\pm 6°$ deviations) in the centre and side regions of the disc when tested at high temperature, see ODF for C-HT (Fig. 9(c)). Moreover, the R-Cube texture component is remained in the side within 10° deviations. The orientation change and formation of new deformation textures were also observed in T-HT disc; compare the ODFs in Fig. 9(d) and Fig. 2(b). It clear from Fig. 9 (d) that Brass and $(123)<634>$ S texture components have high intensity on the sides of the T-HT disc. Whilst Goss, Brass and S have highest intensities in the centre of the disc with R-Cube has disappeared in the entire disc. It is evident that increasing ductility at 650 °C, facilitated shear on other slip planes, *i.e.*, (111), (100) in addition to (110). This is expected as recently reported in [39], the slip system activation is also dependent on the original texture and individual grain orientations. The Cube and Rotated Cube orientations are known as soft orientations and can provide pure shear without the need for grain rotation during deformation, while Brass is a hard orientation that resists deformation and tend to rotate to activate all octahedral slip systems in order to accommodate the large imposed stress [39]. The soft nature and easy octahedral slip system activation in Cube and Rotated Cube oriented grains also explain their persistence during room temperature SP test. It should be emphasised here, that the stress state variation between the centre area and sides of SP disc caused disappearance of some texture components and formation of new ones.

As shown in Fig. 9(b) and (d), some of the produced deformation texture components in the transition microstructure of SP discs at room and high temperature are similar within 10° deviations. As can be seen from the same Figures the Goss orientation was produced in the centre area of the SP disc and Brass (within

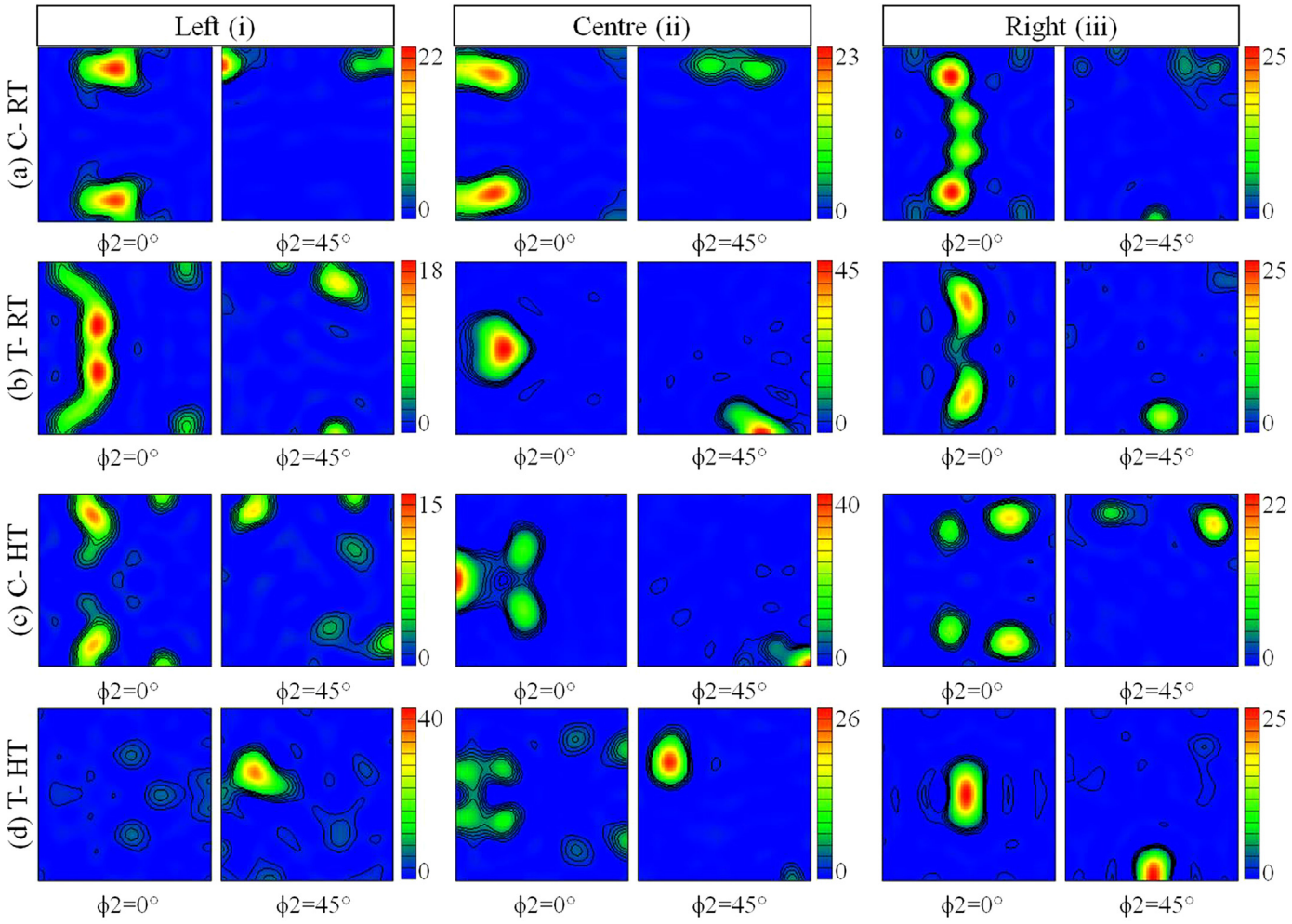

Fig. 9. $\phi 2=0°$ and $\phi 2=45°$ ODF plots for SP samples (a) C-RT, (b) T-RT, (c) C-HT and (d) T-HT sectioned into left, centre and right areas according to Fig. 5.

6–8° deviations) on the sides. This clearly indicates that microstructure parameters are the most important factors in controlling the deformation texture in transition microstructure. This is also reflected in the load/displacement curves for transition microstructure SP discs tested at RT and HT as they both showed good performance, especially in Region I, II and III, see Fig. 3. The better strength for the equiaxed grains and increased strain hardening due to greater number of available slip systems, provided by the hard orientations (*i.e.*, Brass and Goss), in the transition microstructure allowed the T-HT disc to perform better than the rest of the SP discs at RT and HT in the Regions I, II, and III, see Fig. 3(b). However as discussed earlier the boundary region between the equiaxed and columnar grains, see Fig. 2(b), provided a easy path for the primary crack and secondary crack deviation at Region IV which caused sudden and complete failure, see also the fracture surfaces in Fig. 7.

Contrary to observations in the transition microstructure, the deformation texture in the columnar microstructure SP disc at room and high temperatures were different. As can be seen by comparing Fig. 9(a) and (c), the C-RT disc have near Cube orientation ($\pm 7°$) in the centre and Rotated Cube ($\pm 5°$) and Brass ($\pm 4°$) on the sides, whilst the C-HT have Goss and Brass in the centre and Brass, Goss and Rotated Cube with deviations of 15° on the sides. It is clear that the temperature has played a vital role in grain rotations in the columnar microstructure. In summary, the original texture components in both columnar and transition discs have provided readily shear on $<110>$//LD on the side and $<100>$//LD in the centre, thus, there was no need for significant grain rotation during deformation at RT. Furthermore, at HT, the texture components in the C-HT are more close to the ones in T-HT as the disc softens and octahedral slip systems are more easily activated, therefore grain rotation is more likely to occur at HR.

4. Conclusions

Small Punch (SP) test has been successfully applied to the study of deformation behaviour of investment casted IN713C turbine blades sectioned from a diesel turbocharger component. SP discs of columnar grained and mixed equiaxed/columnar (transition) microstructures were tested at Room Temperature (RT) and High Temperature (HT), 650 °C. In addition, Finite Element (FE) analysis of the SP test was also implemented to investigate the role of stress state on the local deformation. The main conclusions of this study are summarised below:

1. The Load/Displacement curves for the SP discs showed that the discs tested at HT yielded much earlier than the discs tested at RT. Furthermore the maximum displacement for the SP discs tested at RT were greater than the SP disc tested at HT. It was evident that equiaxed-columnar transition microstructure could resist further crack propagation, compared to the columnar microstructure at room temperature, and this is closely related to the higher number of grain boundaries in the equiaxed

region.

2. Secondary crack propagation occurred more readily at HT in the columnar microstructure with cracks propagating in all directions, this resulted in greater load reduction in Region IV followed by eventual complete failure shortly after reaching Region V. In the transition microstructure there was immediate failure after Region V at the columnar/equiaxed microstructural interface. It is shown that disc microstructure greatly determines crack propagation and that the boundary between equiaxed and columnar regions facilitated rapid crack propagation and caused sudden failure without necking, shown by the absence of Region V in the strain displacement curve. Conversely the columnar microstructure allowed a decrease in the applied load in Region V that resulted in typical necking before complete failure of the columnar disc.
3. IPF maps and SEM images of tested SP cross sections all showed a change in orientation under deformation in the bulk of the large through thickness grains as well as severe deformation banding. The regions of greatest orientation change have been linked to those areas of highest deformation and occurred at the side of the punch head contact region.
4. Although the microstructural changes occurred during deformation in both the transition and columnar discs, the existing soft orientations of Cube and Rotated Cube in the original microstructure provided $<100>$//LD texture enhancement and pure shear on the $<110>$ direction without rotation of the entire grains at RT. Whereas, at HT orientation changes and grain rotations were observed during the test where the increasing ductility at 650 °C, facilitated primary and any other secondary slip systems, including (111), (100) in addition to (110).
5. It was evident that microstructure parameters are the most influential factors in governing the deformation texture in transition microstructure. Whereas, the temperature was the determining parameter in grain rotation and texture changes for the columnar microstructure.

Acknowledgement

The authors would like to thank EPSRC for the financial support under (EP/L014572/1) EPSRC grant and Cummins Turbo Technologies for supplying the materials. Special thanks to Dr. Sean Winwood from Cummins Turbo Technology, Huddersfield, UK for his support and useful discussion throughout this project.

References

[1] L. Kunz, P. Lukas, R. Konecna, S. Fintova, Int. J. Fatigue 41 (2012) 47–51.
[2] F. Binczyk, J. Śleziona, Arch. Found. Eng. 9 (2009) 109–112.
[3] W.J. Chen, Mech. Syst. Signal Process. 29 (2012) 77–89.
[4] J. Telesman, P. Kantzos, J. Gayda, P.J. Bonacuse, A. Prescenzi, TMS, 2004, pp. 215–224.
[5] D. Pieczaba, A. Jach, Arch. Met. Mater. 55 (2010).
[6] D. Hartman, U. Muerrle, G. Reber, Metall 5 (1992) 443–447.
[7] A. Sabau., S. Viswanathan, Mater. Sci. Eng. A 362 (2003) 125–134.
[8] L. Kunz, P. Lukáš, R. Konečná, Int. J. Fatigue 32 (2010) 908–913.
[9] S. Suresh, Fatigue of Materials, Second edition, Cambridge University Press, Cambridge, 1998.
[10] N. Boutarek, D. Saidi, M.A. Acheheb, M. Iggui, S. Bouterfaia, Mater. Charact. 59 (2008) 951–956.
[11] B. Lin, L.G. Zhao, J. Tong, H.J. Christ, Mater. Sci. Eng. A 527 (2010) 3581–3587.
[12] B. Lin, L.G. Zhao, J. Tong, Eng. Fract. Mech. 78 (2011) 2174–2192.
[13] D. Turan, D. Hunt, D.M. Knowles, Mater. Sci. Technol. 23 (2) (2007) 183–188.
[14] H.T. Pang, P.A.S. Reed, Int. J. Fatigue 25 (2003) 1089–1099.
[15] F. Daus, H.Y. Li, G. Baxter, S. Bray, P. Bowen, Mater. Sci. Technol. 23 (12) (2007) 1424–1426.
[16] D.M. Knowles, D.W. Hunt, Metall. Mater. Trans. A 33A (2002) 3165–3172.
[17] K. Turba, B. Gülçimen, Y.Z. Li, D. Blagoeva, P. Hähner, R.C. Hurst, Eng. Fract. Mech. 78 (2011) 2826–2833.
[18] V. Bicego, H. Rantala, J. Klaput, G. Stratford, F. Persio, R. Hurst, The Small Punch Test Method: Results From a European Creep Testing Round Robin, EPERC TTF5, EPERC Technical Report Nr. 2, 2003.
[19] B. Gülçimen, A. Durmuş, S. Ülkü, R.C. Hurst, K. Turba, P. Hähner, Int. J. Press. Vessel. Pip. 105–106 (2013) 28–35.
[20] Code of Practice for "Small Punch Test Method for Metallic Materials", CEN Workshop Agreement, CWA 15627:2007, 2007.
[21] D. Gelmedin, K.-H. Lang, Prcedia Eng. 2 (1) (2010) 1343–1352.
[22] A. Wisniewski, J. Beddoes, Mater. Sci. Eng. A 510–511 (2009) 266–272.
[23] H.U. Hong, S.W. Nam, J. Mater. Sci. 38 (2003) 1535–1542.
[24] M. Tanaka, H. Iizuka, F. Ashihara, Trans. ISIJ 28 (1988) 129–135.
[25] T. Garcia, C. Rodriguez, F. Belzunce, C. Suarez, J. Alloy. Compd. 582 (2014) 708–717.
[26] Y. Ruan, P. Spätig, M. Victoria, J. Nucl. Mater. 307–311 (2002) 236–239.
[27] E. Fleury, J.S. Ha, Int. J. Press. Vessel. Pip. 75 (1998) 699–706.
[28] C. Rodríguez, J. García, E. Cárdenas, C. Betegón, Mechanical properties characterization of heat-affected zone using the small punch test, Weld. J. 88 (2009) 188–192.
[29] J. Jai-Man Baik, O. Kameda, Buck, Scripta. Met. 17 (1983) 1443–1447.
[30] X. Mao, M. Saito, H. Takahashi, Scr. Met. Mater. 25 (1991) 2481–2485.
[31] S.P. Singh, S. Bhattacharya, D.K. Sehgal, Eng. Fail. Anal. 39 (2014) 207–220.
[32] Y.S. Chang, J.-M. Kim, J.B. Choi, Y.J. Kim, M.C. Kim, B.S. Lee, Eng. Fract. Mech. 75 (2008) 3413–3427.
[33] S.D. Norris, J.D. Parker, Inst. Mater. (1995) 163–170.
[34] ANS 5391E, Aerospace Material Specification, SAE International, 1996.
[35] Haynes Alloy No. 713C, Data Sheet F-30, 1960, 154A.
[36] D.T. Blagoeva, R.C. Hurst, Mater. Sci. Eng. A 510–511 (2009) 219–223.
[37] F.J. Humphreys, M. Hatherly, Recrystallization and Related Annealing Phenomena, First ed., Pergamon Press, Oxford, 1995.
[38] H.-R. Wenk, P. Van Houtte, Rep. Prog. Phys. 67 (2004) 1367–1428.
[39] S. Birosca, F. Di Gioacchino, S. Stekovic, M. Hardy, Acta Mater. 74 (2014) 110–124.